JAM CM Journal of Applied Mathematics and Computational Mechanics 2026, 25(2), 83-97
www.amcm.pcz.pl p-ISSN 2299-9965
DOI: 10.17512/jamcm.2026.2.06 e-ISSN 2353-0588

HYDRODYNAMIC EQUILIBRIA WITH ALIGNED FORCE-FREE MAGNETIC FIELDS FOR SOLAR STRUCTURE MODELING

Eman Hussain, Doaa Ibrahim, Omar El-Kalaawy, Salah Moawad*

Mathematics and Computer Science Department, Faculty of Science, Beni-Suef University, Egypt
dr.eman.taha@science.bsu.edu.eg, doaa.ahmed@science.bsu.edu.eg, ohkalawy7@gmail.com
salahmoawad@science.bsu.edu.eg

Received: 18 October 2025; Accepted: 21 April 2026

Abstract. We present analytical magnetohydrodynamic (MHD) equilibria constructed through Euler potentials (EPs) under aligned force-free magnetic fields (FFMFs). Two classes of solutions are developed by introducing different functional dependencies for the governing free function, resulting in distinct velocity and magnetic field configurations. The equilibria capture key properties of coronal and prominence plasmas. Analysis of the figures shows how variations in the functional form influence the spatial distribution of kinetic energy, with quadratic and exponential profiles producing a stronger concentration near the lower boundary, which suggests enhanced flow stabilization. The squared velocity field highlights the importance of energy localization in determining equilibrium characteristics. These results extend earlier approaches to steady-state MHD equilibria and provide a theoretical framework for understanding plasma structuring in solar and astrophysical environments within an idealized incompressible MHD approximation.

MSC 2010: *76W05, 76B25, 76B47, 76B70, 76U05*
Keywords: *magnetohydrodynamics, force-free fields, Euler potentials, coronal loops, solar prominences*

1. Introduction

MHD equilibria play a fundamental role in understanding plasma confinement and stability in both laboratory and astrophysical environments [1-3]. Many classical studies have employed axisymmetric or cylindrical configurations within the Grad-Shafranov framework, which has been widely used to model tokamak equilibria and related plasma systems [4-8]. Extensions of the Grad-Shafranov equation to treat non-axisymmetric magnetic fields have also been developed [9]. In addition, several numerical approaches have been proposed to compute more general MHD equilibria, including spectral and modern regularization-based methods (e.g., Belien et al. [10];

* Corresponding author

Huang et al. [11]). A number of analytical solutions are known, including the classical solutions of Meyer and Schmidt [12] and the later formulation by Lortz [13].

However, deriving analytical 3D MHD solutions without assuming spatial symmetry remains a formidable challenge, with only limited success using either numerical methods or symmetry-based reductions [14-16].

In astrophysics, especially in solar contexts, magnetic fields are often force-free due to the dominance of magnetic energy over kinetic and thermal energies [17]. Realistic configurations such as sunspots and coronal loops demand nonlinear approaches with spatially varying force-free parameters [18]. Existing analytical models largely assume constant force-free parameter, limiting their applicability to observed solar structures where magnetic complexity and gravitational influence are significant.

The novelty of this work lies in the development of exact 3D solutions for incompressible, inviscid MHD flows with nonlinear force-free magnetic fields (NLFFMFs) in a gravitational field. The incompressibility assumption is adopted here as an analytical simplification that allows tractable exact solutions while still capturing key features of magnetically dominated plasma environments such as solar coronal structures [19]. The solutions should therefore be interpreted as idealized analytical models that help reveal the role of magnetic topology and flow structure in solar plasma configurations. By introducing EPs, tools previously underutilized in fully 3D solar modeling, we formulate a self-consistent class of solutions for velocity, magnetic field, current density, and pressure. While EPs have been explored in magnetospheric and limited solar contexts [20], their integration into 3D nonlinear MHD equilibrium theory is new.

Our examples demonstrate that this approach captures key features of solar prominences, coronal loops, and sunspots. This work thus provides a more flexible and analytically tractable framework for modelling complex solar magnetic environments, offering a meaningful extension beyond prior symmetry-constrained or numerically limited studies.

2. Fundamental equations of field-aligned incompressible MHD equilibrium

In the present formulation, the alignment between the velocity and magnetic field naturally arises from the assumption of field-aligned flows, which is commonly adopted in steady MHD equilibrium models. Under this assumption, the velocity is taken to be parallel to the magnetic field, i.e., $\mathbf{v} \parallel \mathbf{B}$, which ensures that the flow does not distort magnetic field lines and remains consistent with the frozen-in condition of ideal MHD. Such configurations are physically relevant in magnetically dominated (low-β) plasma environments, such as solar coronal loops and prominences, where plasma flows are frequently observed to follow magnetic field lines.

The fundamental equations governing field-aligned, incompressible MHD equilibrium are derived from the conservation laws of fluid dynamics and electromagnetism, specifically incorporating Gauss's law, Faraday's law, and Ohm's law:

$$\rho(\mathbf{v}\cdot\nabla)\mathbf{v} = -\nabla P - \rho\nabla\Theta + \mathbf{J}\wedge\mathbf{B}, \tag{1}$$

the continuity equation with incompressibility condition

$$\mathbf{v}\cdot\nabla\rho = 0,\ \nabla\cdot\mathbf{v} = 0, \tag{2}$$

$$\nabla\cdot\mathbf{B} = 0, \tag{3}$$

$$\nabla\wedge\mathbf{E} = 0, \tag{4}$$

$$\mathbf{E} + \mathbf{v}\wedge\mathbf{B} = 0, \tag{5}$$

Throughout this work, we adopt the standard notation: **v** for fluid velocity, P for gas pressure, ρ for fluid density, Θ for gravitational potential, **J** for current density, **B** for magnetic field, and **E** for electric field.

Using the vector identity:

$$(\mathbf{v}\cdot\nabla)\mathbf{v} = \frac{1}{2}\nabla(v^2) + (\nabla\wedge\mathbf{v})\wedge\mathbf{v}, \tag{6}$$

equation (1) becomes

$$\rho\nabla\left(\frac{v^2}{2}\right) - \rho\mathbf{v}\wedge\boldsymbol{\Omega} + \nabla P + \rho\nabla\Theta - \mathbf{J}\wedge\mathbf{B} = 0, \tag{7}$$

where $\boldsymbol{\Omega}\equiv\nabla\wedge\mathbf{v}$ stands as usual for the vorticity field.
The nonlinear FFMFs are described by $\mathbf{J} = \lambda\mathbf{B}$, where $\lambda = \lambda(x,y,z)$, i.e.,

$$\mathbf{J}\wedge\mathbf{B} = 0. \tag{8}$$

Using Eq. (8), Eq. (7) leads to

$$\nabla\left(P + \frac{1}{2}\rho v^2 + \rho\Theta\right) - \rho\mathbf{v}\wedge\boldsymbol{\Omega} - \left(\Theta + \frac{v^2}{2}\right)\nabla\rho = 0 \tag{9}$$

From Eq. (2), the dot product of Eq. (9) by the velocity field yields

$$\mathbf{v}\cdot\nabla\left(P + \frac{1}{2}\rho v^2 + \rho\Theta\right) = 0. \tag{10}$$

Therefore, a class of solution (particular case of the general solution) can be obtained from Eqs. (2) and (10) by putting

$$P + \frac{1}{2}\rho v^2 + \rho\Theta = K(\rho), \tag{11}$$

where $K(\rho)$ is a function of ρ.
Substituting by Eq. (11) into Eq. (9), we get

$$\left(\frac{dK}{d\rho} - \Theta - \frac{v^2}{2}\right)\nabla\rho - \rho\mathbf{v}\wedge\mathbf{\Omega} = 0. \tag{12}$$

The dot product of Eq. (12) by $\mathbf{\Omega}$ yields

$$\mathbf{\Omega}\cdot\nabla\rho = 0. \tag{13}$$

3. General formulation of 3D MHD equilibria

Building on the analysis presented above, we construct a class of 3D solutions corresponding to the flow configurations discussed in Section 2.

To construct 3D magnetic field configurations, we employ EP, which provide a convenient representation of divergence-free magnetic fields in the form $\mathbf{B} = \alpha(\rho,\xi)f(\rho,\xi)\nabla\xi\wedge\nabla\rho$, where ρ and ξ are scalar functions. This formulation is particularly useful in analytical MHD equilibria, as it naturally satisfies $\nabla\cdot\mathbf{B} = 0$ and allows flexible construction of complex magnetic topologies. In this framework, the velocity field is assumed to be aligned with the magnetic field $\mathbf{v}\parallel\mathbf{B}$, consistent with the field-aligned flow assumption discussed earlier.

$$\begin{aligned}
&\mathbf{v} = f(\rho,\xi)\nabla\xi\wedge\nabla\rho,\ \ \xi\equiv\xi(x,y,z),\ \ \rho\equiv\rho(x,y,z),\\
&\mathbf{B} = \alpha\mathbf{v}, \alpha = \alpha(\rho,\xi),\ \ \mathbf{J} = \lambda\mathbf{B},\ \ \lambda = \lambda(\rho,\xi),\\
&K = \int\left(\Theta + \rho f(\mathbf{\Omega}\cdot\nabla\xi) + \frac{v^2}{2}\right)d\rho,\\
&P = K(\rho) - \frac{1}{2}\rho v^2 - \rho\Theta,\ \ K(\rho)\geqslant\frac{1}{2}\rho(v^2+2\Theta)
\end{aligned} \tag{14}$$

with

$$\frac{\partial f}{\partial\xi}||\nabla\xi\wedge\nabla\rho||^2 = f\nabla\rho\cdot\nabla\wedge(\nabla\xi\wedge\nabla\rho). \tag{15}$$

In what follows we prove the solutions introduced in Eqs. (14) and (15). Using $\mathbf{v} = f\nabla\xi\wedge\nabla\rho$ in Eq. (2), we have

$$\mathbf{v}\cdot\nabla\rho = f(\rho,\xi)\nabla\rho\cdot(\nabla\xi\wedge\nabla\rho) = 0. \tag{16}$$

Using the following identity

$$\nabla\cdot(\mathbf{L}\wedge\mathbf{M}) = \mathbf{M}\cdot(\nabla\wedge\mathbf{L}) - \mathbf{L}\cdot(\nabla\wedge\mathbf{M}), \tag{17}$$

we have,

$$\nabla\cdot\mathbf{v} = f\nabla\cdot(\nabla\xi\wedge\nabla\rho) + \left(\frac{\partial f}{\partial\xi}\nabla\xi + \frac{\partial f}{\partial\rho}\nabla\rho\right)\cdot(\nabla\xi\wedge\nabla\rho) = 0. \tag{18}$$

Thus, Eq. (2) holds true.

To demonstrate that the momentum equation is satisfied, it is sufficient to verify that its equivalent form, given by Eq. (12), holds. To this end, we make use of the following vector identity

$$\mathbf{L} \wedge (\mathbf{M} \wedge \mathbf{N}) = (\mathbf{L} \cdot \mathbf{N})\mathbf{M} - (\mathbf{L} \cdot \mathbf{M})\mathbf{N}, \tag{19}$$

to calculate $\boldsymbol{\Omega} \wedge \mathbf{v}$ as

$$\boldsymbol{\Omega} \wedge \mathbf{v} = f\boldsymbol{\Omega} \wedge (\nabla\xi \wedge \nabla\rho) = f[(\boldsymbol{\Omega} \cdot \nabla\rho)\nabla\xi - (\boldsymbol{\Omega} \cdot \nabla\xi)\nabla\rho]. \tag{20}$$

Substituting Eq. (20) in Eq. (12) yields

$$\left(\frac{dK}{d\rho} - \Theta - \frac{1}{2}v^2\right)\nabla\rho + \rho f[(\boldsymbol{\Omega} \cdot \nabla\rho)\nabla\xi - (\boldsymbol{\Omega} \cdot \nabla\xi)\nabla\rho] = 0. \tag{21}$$

Using Eq. (13), we get

$$\left(\frac{dK}{d\rho} - \Theta - \frac{1}{2}v^2 - \rho f(\boldsymbol{\Omega} \cdot \nabla\xi)\right)\nabla\rho = 0. \tag{22}$$

Comparing Eq. (22) with the expression for the gravitational potential $\Theta(x, y, z)$ given in Eq. (14), we confirm Eq. (1) is satisfied. What remains is to verify the compatibility condition expressed in Eq. (15), which we establish in the following analysis.
Applying Eq. (14) together with Eq. (19), we obtain the following result:

$$\begin{aligned}\boldsymbol{\Omega} &= \nabla \wedge \mathbf{v} \\ &= f\nabla \wedge (\nabla\xi \wedge \nabla\rho) + (\nabla f \cdot \nabla\rho)\nabla\xi - (\nabla f \cdot \nabla\xi)\nabla\rho.\end{aligned} \tag{23}$$

Since $f = f(\xi, \rho)$, hence

$$\nabla f \cdot \nabla\rho = \frac{\partial f}{\partial \rho}||\nabla\rho||^2 + \frac{\partial f}{\partial \xi}\nabla\xi \cdot \nabla\rho, \tag{24}$$

$$\nabla f \cdot \nabla\xi = \frac{\partial f}{\partial \xi}||\nabla\xi||^2 + \frac{\partial f}{\partial \rho}\nabla\rho \cdot \nabla\xi. \tag{25}$$

Therefore Eq. (23) becomes

$$\begin{aligned}\Omega = &\left(\frac{\partial \mathrm{f}}{\partial \xi}\nabla\xi \cdot \nabla\rho + \frac{\partial \mathrm{f}}{\partial \rho}||\nabla\rho||^2\right)\nabla\xi + \mathrm{f}\nabla \wedge (\nabla\xi \wedge \nabla\rho) \\ &- \left(\frac{\partial f}{\partial \xi}||\nabla\xi||^2 + \frac{\partial f}{\partial \rho}\nabla\rho \cdot \nabla\xi\right)\nabla\rho.\end{aligned} \tag{26}$$

Taking the scalar product of Eq. (26) by $\nabla\rho$, we get

$$\boldsymbol{\Omega} \cdot \nabla\rho = f\nabla\rho \cdot \nabla \wedge (\nabla\xi \wedge \nabla\rho) + \frac{\partial f}{\partial \xi}[(\nabla\xi \cdot \nabla\rho)^2 - ||\nabla\xi||^2||\nabla\rho||^2]. \tag{27}$$

Using the identity

$$||\mathbf{L} \wedge \mathbf{M}||^2 + (\mathbf{L} \cdot \mathbf{M})^2 = ||\mathbf{L}||^2||\mathbf{M}||^2, \tag{28}$$

Eq. (27) becomes

$$\boldsymbol{\Omega} \cdot \nabla\rho = f\nabla\rho \cdot \nabla \wedge (\nabla\xi \wedge \nabla\rho) - \frac{\partial f}{\partial \xi}||\nabla\xi \wedge \nabla\rho||^2. \tag{29}$$

Using Eqs. (13) and (29), we obtain the compatibility condition presented in Eq. (15), considering a magnetic field aligned with the velocity field, then

$$\mathbf{B} = \alpha\mathbf{v}. \tag{30}$$

Substituting by Eq. (30) into Eq. (3), we get

$$\nabla \cdot \mathbf{B} = \nabla \cdot (\alpha\mathbf{v}) = \alpha(\nabla \cdot \mathbf{v}) + \mathbf{v} \cdot \nabla\alpha = 0. \tag{31}$$

Using the equation of incompressibility, we get

$$\mathbf{v} \cdot \nabla\alpha = 0. \tag{32}$$

Using Eq. (14), we have

$$f(\rho, \xi)(\nabla\xi \wedge \nabla\rho) \cdot \nabla\alpha = 0, \tag{33}$$

hence,

$$\alpha = \alpha(\rho, \xi). \tag{34}$$

Substituting Eq. (30) into Eq. (5), we get

$$\mathbf{E} = 0, \tag{35}$$

so, Eq. (5) is satisfied.
Since $\mathbf{J} = \nabla \wedge \mathbf{B}$ and $\mathbf{J} = \lambda\mathbf{B}$, then we have

$$\nabla \wedge \mathbf{B} = \lambda\mathbf{B}. \tag{36}$$

Taking the divergence to Eq. (36), we have

$$\nabla \cdot (\lambda\mathbf{B}) = \lambda(\nabla \cdot \mathbf{B}) + \mathbf{B} \cdot \nabla\lambda = 0. \tag{37}$$

From Eq. (3), we get

$$\mathbf{B} \cdot \nabla\lambda = 0. \tag{38}$$

Using the expression of the magnetic field, we have

$$\alpha f(\rho, \xi)(\nabla\xi \wedge \nabla\rho) \cdot \nabla\lambda = 0. \tag{39}$$

Therefore,

$$\lambda = \lambda(\rho, \xi), \tag{40}$$

which completes the proof of Eqs. (14) and (15). ■

4. Plasma flow in an exponentially stratified atmosphere

We consider the EP and density profile

$$\xi(x, y, z) = e^{a_1 x + b_1 y + c_1 z}, \ \rho(z) = \rho_0 e^{-z/H}, \tag{41}$$

where a_1, b_1, and c_1 control the orientation of the ξ-surfaces, ρ_0 is the density at $z = 0$, and H is the density scale height.
The gravitational potential is taken in the local linearized form

$$\Theta(z) = g_{\odot} z. \tag{42}$$

This form is appropriate for coronal structures at heights much smaller than the solar radius, with $g_{\odot} \approx 274 \ \mathrm{m\,s^{-2}}$.

From Eq. (15), the compatibility condition yields

$$f(\rho, \xi) = \frac{F(\rho)}{\xi}. \tag{43}$$

We adopt the scaling

$$F(\rho) = F_0 \, \rho^p, \tag{44}$$

where F_0 and p are constants.
The vector

$$\mathbf{W} = \nabla\xi \times \nabla\rho \tag{45}$$

becomes, for the choice (41),

$$\mathbf{W} = \frac{\rho(z) \, \xi(x, y, z)}{H} \, (-b_1, a_1, 0). \tag{46}$$

The velocity is then

$$\mathbf{v} = f\mathbf{W} = \frac{F_0}{H} \rho^{p+1} (-b_1, a_1, 0), \tag{47}$$

which is purely horizontal and decays exponentially with height. Its magnitude is

$$v^2(z) = \frac{F_0^2}{H^2} (a_1^2 + b_1^2) \, \rho(z)^{2(p+1)}. \tag{48}$$

The vorticity $\mathbf{\Omega} = \nabla \times \mathbf{v}$ leads to

$$\mathbf{\Omega} \cdot \nabla\xi = \frac{F_0}{H^2}(a_1^2 + b_1^2)(p+1)\,\xi\,\rho^{p+1}. \tag{49}$$

Thus,

$$\rho\, f(\mathbf{\Omega} \cdot \nabla\xi) = \frac{F_0^2}{H^2}(a_1^2 + b_1^2)(p+1)\,\rho^{2p+2}. \tag{50}$$

From Eq. (14),

$$K(\rho) = \int \left[\Theta + \rho\, f(\mathbf{\Omega} \cdot \nabla\xi) + \frac{1}{2}v^2\right] d\rho. \tag{51}$$

Expressing Θ in terms of ρ via $z = -H\ln(\rho/\rho_0)$ gives

$$\Theta(\rho) = -g_\odot H \ln\left(\frac{\rho}{\rho_0}\right). \tag{52}$$

The integrand becomes

$$-g_\odot H \ln\left(\frac{\rho}{\rho_0}\right) + \frac{F_0^2}{H^2}(a_1^2 + b_1^2)\left(p + \frac{3}{2}\right)\rho^{2p+2}. \tag{53}$$

Integrating term-by-term yields

$$K(\rho) = -g_\odot H\left[\rho \ln\left(\frac{\rho}{\rho_0}\right) - \rho\right] + \frac{F_0^2(a_1^2 + b_1^2)}{2H^2}\,\rho^{2p+3} + K_0 \tag{54}$$

where K_0 is an integration constant.
Using Eq. (14),

$$P = K(\rho) - \frac{1}{2}\rho v^2 - \rho\Theta, \tag{55}$$

and substituting (54), (47), and (42), all nonlinear ρ^{2p+3} terms cancel, leaving

$$P(\rho) = g_\odot H\rho + K_0. \tag{56}$$

For $K_0 = 0$, the pressure is directly proportional to the density, consistent with a hydrostatic atmosphere.

The exponential forms adopted for ξ and ρ in this example are not arbitrary but are physically motivated by common solar atmospheric models. The density profile $\rho(z) = \rho_0 e^{-z/H}$ represents an isothermal gravitationally stratified plasma, frequently used for the corona and prominences, where the scale height H depends on temperature and solar gravity [21]. The EP $\xi = e^{a_1 x + b_1 y + c_1 z}$ produces planar magnetic-flux

surfaces whose inclination can be adjusted via a_1, b_1, c_1 to mimic different orientations of coronal loops or filament channels. The local gravitational potential $\Theta(z) = g_\odot z$ is a valid approximation for heights that are small compared with the solar radius.

The resulting velocity field $\mathbf{v}$ is purely horizontal and decreases exponentially with height, consistent with the observed reduction of plasma flow speeds in the upper corona [22]. The vorticity term $\boldsymbol{\Omega} \cdot \nabla\xi$ takes a compact analytic form proportional to ρ^{p+1}, simplifying the computation of $K(\rho)$ and $P(\rho)$. The derived pressure distribution, $P(\rho) = g_\odot H\rho + K_0$, is linear in ρ, indicating a hydrostatic balance. This is physically consistent with the force-free condition ($\mathbf{J} \times \mathbf{B} = 0$), under which the Lorentz force vanishes and the momentum equation reduces to a balance between the pressure gradient and gravity.

5. Three-dimensional NFFF with hyperbolic density core

We now consider a second family of exact equilibria, obtained by choosing the EPs

$$\xi(x,y,z) = e^{a_1x+b_1y+c_1z},\ \rho(x,y,z) = \cosh(S),\ S = a_2x + b_2y + c_2z. \quad (57)$$

The gradients of ξ and ρ are linearly independent for generic (a_i, b_i, c_i), ensuring a non-trivial $\mathbf{W} = \nabla\xi \times \nabla\rho$ with all three components generally nonzero.
From the definitions in Section 2, the components of $\mathbf{L} := (l_1, m_1, n_1)$ are

$$l_1 = b_1c_2 - c_1b_2,\quad m_1 = c_1a_2 - a_1c_2,\ n_1 = a_1b_2 - b_1a_2, \quad (58)$$

and

$$L^2 = l_1^2 + m_1^2 + n_1^2. \quad (59)$$

The function $f(\rho, \xi)$ satisfying Eq. (15) takes the separable form

$$f(\rho,\xi) = \frac{1}{\xi\, R(\rho)}, \quad (60)$$

with $R(\rho)$ to be specified.
The velocity field is

$$\mathbf{v}(x,y,z) = \frac{\sinh S}{R(\rho)}\,\mathbf{L}. \quad (61)$$

The magnetic field in the nonlinear force-free formulation is

$$\mathbf{B}(x,y,z) = \frac{\alpha(\rho,\xi)}{R(\rho)}\,\mathbf{L}\sinh S, \quad (62)$$

and the associated current density is

$$\mathbf{J}(x,y,z) = \frac{\alpha(\rho,\xi)\,\lambda(\rho,\xi)}{R(\rho)}\,\mathbf{L}\,\sinh S. \tag{63}$$

Here $\alpha(\rho,\xi)$ and $\lambda(\rho,\xi)$ are related through the force-free condition $\nabla\times\mathbf{B}=\lambda\,\mathbf{B}$, which constrains their functional form.
From Eq. (63), with $R(\rho)=R_0>0$ (constant) and $\Theta(\rho)=\Theta_0+g_0\,\rho$ (gravity depending only on ρ for compatibility), and using

$$\cosh S=\rho,\ \ \sinh^2 S=\rho^2-1, \tag{64}$$

the Bernoulli equation reduces to

$$\frac{dK}{d\rho}=\Theta_0+g_0\,\rho+\frac{L^2}{R_0^2}\left[\rho^2-\frac{\rho(\rho^2-1)}{R_0}+\frac{1}{2}\right]. \tag{65}$$

Integrating in ρ yields

$$K(\rho)=K_0+\Theta_0\,\rho+\frac{g_0}{2}\,\rho^2+\frac{L^2}{R_0^2}\left(\frac{\rho^3}{3}-\frac{\rho^4}{4R_0}+\frac{\rho}{2}\right), \tag{66}$$

where K_0 is an integration constant.
From Eq. (64), the pressure is

$$P(\rho)=K(\rho)-\rho\,K'(\rho)+\frac{\rho\,L^2}{R_0^2}\left[\rho^2-\frac{\rho^2-1}{R_0}\right]. \tag{67}$$

Substituting $K(\rho)$ and simplifying gives

$$P(\rho)=P_0-\frac{g_0}{2}\,\rho^2+\frac{L^2}{2R_0^3}\,\rho^2-\frac{L^2}{4R_0^3}\,\rho^4, \tag{68}$$

with $P_0\equiv K_0$ representing a constant background pressure.

The configuration represents a NLFFM structure embedded in a stratified solar atmosphere, where the density ρ forms a dense core along $S=0$ and decreases outward. The density distribution seen in prominences and coronal loops is replicated by this hyperbolic profile, $\rho=\cosh S$, which has smooth lateral decay along field lines and center augmentation [23]. These characteristics align with force-free prominence models [24], in which curved field lines provide magnetic support for dense cores. Straight and arched prominence threads can be modeled without singularities in pressure or density thanks to the hyperbolic function's symmetry.

The field-line bundle's orientation is set by the vector $\mathbf{L}=(l,m,n)$. The twisted field lines with finite parallel current density that result from a nonzero **L** imply that $\nabla\xi$ and $\nabla\rho$ are not parallel. This is consistent with NLFFF structures deduced from

magnetograms [25], where magnetic twist and shear are indicated by the spatially varying force-free parameter λ.

The equilibrium between gravity, pressure gradients, and magnetic tension is controlled by the Bernoulli function $K(\rho)$. The conflict between magnetic tension and pressure forces under gravitational stratification is shown in the pressure law in Eq. (68), which exhibits quadratic rise and quartic decrease with ρ. Stable ($P > 0$) or unstable ($P < 0$) structures that are pertinent to pre-eruptive prominences can be represented by adjusting g_0 and R_0 [26].

In contrast to the potential-field situation in Section 4, setting $R(\rho)$ constant results in a field with spatially variable $\lambda(\rho, \xi) \neq 0$ that can store magnetic helicity and free energy. When kink or torus instabilities form, such fields may appear before eruptions [27]. According to low-β coronal conditions, the solution meets the NLFF condition $\nabla \wedge \mathbf{B} = \lambda(\rho, \xi)\mathbf{B}$ [19]. Localized current concentrations along twisted flux bundles are revealed by nonlinear force-free extrapolations, which are consistent with the spatial variation of λ [25].

6. Results and discussion

The vertical density profiles $\rho(z)$ for various scale heights H in Eq. (41) are shown in Figure 1. As expected from the exponential dependence, the density decreases monotonically with altitude, with larger values of H producing slower decay rates. For example, at $z = 10$, the density drops to nearly $\rho \approx 0.02$ when $H = 2$, but remains as high as $\rho \approx 0.37$ for $H = 10$. This behavior highlights the role of gravitational stratification in plasma confinement: smaller H values correspond to cooler or more compact plasmas, whereas larger H values reflect hotter or more extended structures. Such exponential stratification has been widely recognized in MHD modeling of astrophysical and laboratory plasmas.

In Figure 2, the squared velocity profiles are shown for different values of the exponent parameter p in Eq. (44). All profiles decrease sharply with height, with the most rapid decay observed for larger p. Near the base ($z \leq 1$), the velocity squared is close to 0.05, while by $z = 5$ the values have dropped below 0.005 for $p = 1.5$. Physically, this indicates that steeper exponents accelerate the damping of flow with altitude, which is consistent with the stabilizing role of gravity-modified flows in stratified plasmas. Similar damping behaviors have been reported in studies of steady and stratified MHD equilibria.

The squared velocity field in Eq. (61) for various functional forms of $R(\rho)$ at $y = 0$ and $z = 0$ is shown in Figure 3. The highest velocity amplitudes are obtained in the unshifted case $R(\rho) = \rho$, where $v^2 \approx 0.32$ at $x = \pm 3$. The velocity field steadily decreases across the domain as constant shifts ($R(\rho) = \rho + 0.5, \rho + 1, \rho + 1.5$) are applied, reaching only $v^2 \approx 0.16$ for $R(\rho) = \rho + 1.5$ at the same position. This demonstrates how sensitive equilibrium velocity structures are to functional changes in the radial dependency and emphasizes the relationship between density

profiles and flow strength. These findings are in line with other symmetry-based approaches to MHD equilibria research, which emphasize the role of functional invariants in determining the velocity and magnetic field configurations [3, 16].

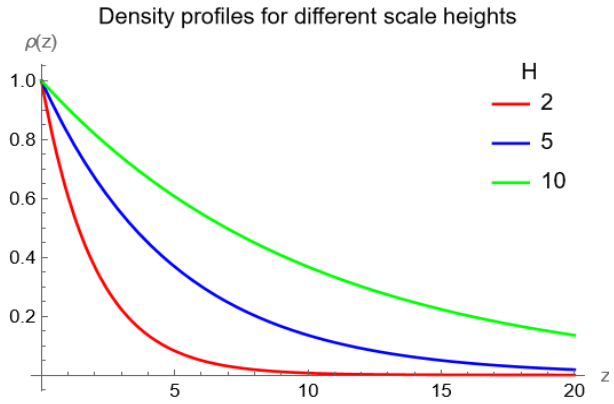

Fig. 1. Vertical density profile $\rho(z)$ on a semilogarithmic scale. The exponential decrease with scale height H produces a straight line in log coordinates, highlighting the role of gravitational stratification. Different values of H correspond to different thermal conditions, with larger H indicating hotter or more extended plasmas

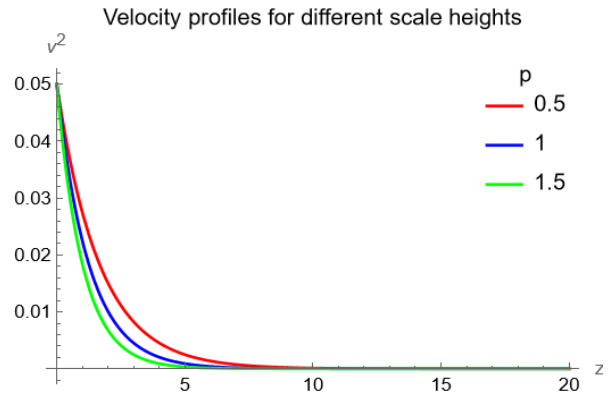

Fig. 2. Square of velocity profiles for different values of the exponent parameter p in Eq. (44)

Figure 3 illustrates how the kinetic-energy distribution is controlled by the selection of $R(\rho)$. While quadratic and exponential forms localize energy close to the lower boundary, increasing shear and possible instability, linear and inverse forms create broader, more stable profiles. Therefore, stability is directly impacted by $R(\rho)$ by energy localization.

The magnetic structure is shown in Figure 4, with flow-aligned field lines that are ordered and force-free. These equilibria extend earlier work [6, 7] and apply to coronal loops and prominences [23-26], along with stratification (Fig. 1), damping (Fig. 2), and sensitivity to $R(\rho)$ (Fig. 3).

Overall, density and flow behavior are controlled by the parameters H, p, and $R(\rho)$, providing a versatile analytical framework in line with previous research [4].

Magnetic hoop-stress limitations are reflected in Figure 4, where the pressure profile from Eq. (28) exhibits a limiting quartic behavior at high ρ and a stabilizing quadratic term at low ρ [28, 29]. By varying g_0 and R_0, structures can either develop instability sites ($P < 0$) or stay stable ($P > 0$).

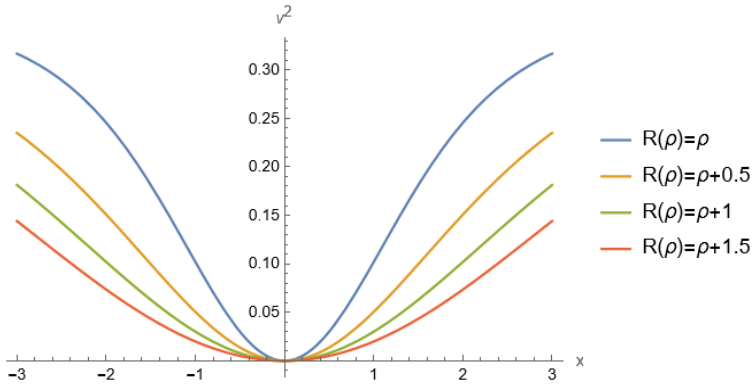

Fig. 3. The distribution of kinetic energy density for various functional forms of $R(\rho)$ at $y = 0$ and $z = 0$ is represented by the squared velocity field

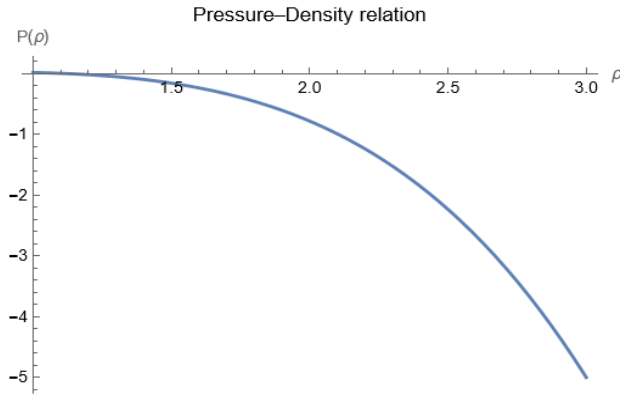

Fig. 4. Equation (28) yields the analytic pressure-density relation $P(\rho)$

7. Conclusions

In this work, Euler potentials were used to explicitly solve the steady MHD equations with aligned FFMFs analytically. The analysis showed that altering the free function's form results in various equilibrium configurations, especially with regard to the distribution of kinetic energy. Increased energy concentration close to the lower boundary was the outcome of quadratic and exponential forms, which might

help stabilize the flow. The inverse and linear forms, on the other hand, generated wider energy distributions, which would have permitted the emergence of instabilities. These results highlight how the choice of free functions affects equilibrium stability characteristics. In addition to their analytical utility, the solutions can be used to analyze structuring in prominence plasmas and solar coronal loops and can be used as standards for numerical magnetohydrodynamic programs. The present solutions are obtained within the incompressible ideal MHD framework, which provides analytically tractable models for magnetically dominated plasma environments.

References

[1] Schmitt, J.C., Andrew, E.C., Anderson, D., & Bader, A. (2025). Magnetohydrodynamic equilibrium and stability properties of the Infinity Two fusion pilot plant. *Journal of Plasma Physics*, *91*(3), 1-39.

[2] Bandyopadhyay, I., Igochine, V., Sauter, O., Sabbagh, S.A., Park, J.A., Nardon, E., Villone, F., Maraschek, M., Pautasso, G., & Eidietis, N. (2025). MHD, disruptions and control physics: Chapter 4 of the special issue: on the path to tokamak burning plasma operation. *Nuclear Fusion*, *65*(7), 076028.

[3] Goedbloed, J.P. (2018). MHD instabilities in astrophysical plasmas: very different from MHD instabilities in tokamaks. *Plasma Physics and Controlled Fusion*, *60*(1), 014001.

[4] Haolong, L., & Ping, Z. (2021). Solving the Grad-Shafranov equation using spectral elements for tokamak equilibrium with toroidal rotation. *Computer Physics Communications*, *260*, 107264.

[5] Kaltsas, D.A., & Throumoulopoulos, G.N. (2022). Neural network tokamak equilibria with incompressible flows. *Physics of Plasmas*, *29*(2), 022506.

[6] Kuiroukidis, A., & Throumoulopoulos, G.N. (2018). Tokamak equilibria with non-parallel flow in a triangularity-deformed axisymmetric toroidal coordinate system. *Heliyon*, *4*(1), e00499.

[7] Rodrigues, P., & Coroado, A. (2018). Local up-down asymmetrically shaped equilibrium model for tokamak plasmas. *Nuclear Fusion*, *58*(10), 106040.

[8] Nikulsin, N., Hoelzl, M., Zocco, A., Lackner, K., & Günter, S. (2019). A three-dimensional reduced MHD model consistent with full MHD. *Physics of Plasmas*, *26*, 102109.

[9] Burby, J.W., Kallinikos, N., & MacKay, R.S. (2020). Generalized Grad-Shafranov equation for non-axisymmetric MHD equilibria. *Physics of Plasmas*, *27*(10), 102504.

[10] Belien, A.J.C., Botchev, M.A., & Goedbloed, J.P. (2002). van der Holst, B., & Keppens, R. FINESSE: Axisymmetric MHD equilibria with flow. *Journal of Computational Physics*, *182*(1), 91-117.

[11] Huang, Y.-M., Hew, J.K.J., Brown, A., & Bhattacharjee, A. (2025). Computation of magnetohydrodynamic equilibria with Voigt regularization. arXiv preprint arXiv:2502.19594.

[12] Meyer, F., & Schmidt, H.U. (1958). Torusartige Plasmakonfigurationen ohne Gesamtstrom durch ihren Querschnitt im Gleichgewicht mit einem Magnetfeld. *Zeitschrift für Naturforschung A*, *13a*, 1005-1010.

[13] Lortz, D. (1970). Über die Existenz toroidaler magnetohydrostatischer Gleichgewichte ohne Rotationstransformation. *Journal of Applied Mathematics and Physics (ZAMP)*, *21*, 196-211.

[14] Wilson, F., & Neukirch, T. (2018). Three-dimensional solutions of the magnetohydrostatic equations for rigidly rotating magnetospheres in cylindrical coordinates. *Geophysical and Astrophysical Fluid Dynamics*, *112*(1), 74-95.

[15] Shehzad, S.A., Hayat, T., & Alsaedi, A. (2016). Three-dimensional MHD flow of Casson fluid in porous medium with heat generation. *Journal of Applied Fluid Mechanics*, *9*, 215-223.

[16] Adem, A.R., & Moawad, S.M. (2017). Exact solutions to several nonlinear cases of generalized Grad-Shafranov equation for ideal magnetohydrodynamic flows in axisymmetric domain. *Zeitschrift für Naturforschung A*, *73*(5), 371-383.

[17] Moawad, S.M., El-Kalaawy, O.H., & Shaker, H.M. (2017). Some axisymmetric equilibria for certain ideal and resistive magnetohydrodynamics with incompressible flows. *Results in Plasmas*, *7*, 3163-3175.

[18] Sheikhahmadi, H. (2022). Schwarzschild black hole perturbed by a force-free magnetic field. *Foundation of Physics*, *52*(93), 1-12.

[19] Gary, G.A. (2001). Plasma beta above a solar active region: Rethinking the paradigm. *Solar Physics*, *203*, 71-86.

[20] Terradas, J., & Neukirch, T. (2023). Three-dimensional solar active region magnetohydrostatic models and their stability using Euler potentials. *Astronomy and Astrophysics*, *671*(A31).

[21] Aschwanden, M.J. (2004). *Physics of the Solar Corona: An Introduction with Problems and Solutions*. Berlin: Springer.

[22] Antolin, P., Vissers, G., Pereira, T.M.D., Rouppe, van der Voort, L., & Scullion, E. (2012). Observing the fine structure of loops through high spatial resolution coronal rain observations with the CRISP instrument at the Swedish Solar Telescope. *Solar Physics*, *280*, 457-474.

[23] Gibson, S.E. (2018). Solar prominences: Theory and models. *Living Reviews in Solar Physics*, *15*(7).

[24] Aulanier, G., & Démoulin, P. (1998). 3-D magnetic configurations supporting prominences. I. The natural presence of lateral feet. *Astrononmy and Astrophysics*, *329*, 1125-1137.

[25] Wiegelmann, T., & Sakurai, T. (2012). Solar force-free magnetic fields. *Living Reviews in Solar Physics*, *9*(5).

[26] Mackay, D.H., Karpen, J.T., Ballester, J.L., Schmieder, B., & Aulanier, G. (2010). Physics of solar prominences: II. Magnetic structure and dynamics. *Space Science Reviews*, *151*, 333-399.

[27] Aulanier, G., Török, T., Démoulin, P., & DeLuca, E.E. (2010). Formation of torus-unstable flux ropes and electric currents in erupting sigmoids. *The Astrophysical Journal*, *708*, 314.

[28] Madjarska, M.S., Wiegelmann, T., Démoulin, P., & Galsgaard, K. (2024). Coronal magnetic field and emission properties of small-scale bright and faint loops in the quiet Sun. *Astronomy and Astrophysics*, *690*, A242.

[29] Gupta, M., Thalmann, J.K., & Veronig, A.M. (2024). Stability of the coronal magnetic field around large confined and eruptive solar flares. *Astronomy and Astrophysics*, *686*, A115.